

Extracting common signal components from the X-ray and optical light curves of GX 339–4: new view for anti-correlation

Tomoki Omama^{1, 2, 3}, Makoto Uemura⁴, Shiro Ikeda⁵, Mikio Morii⁶

¹Department of Physical Science, Hiroshima University, Kagamiyama 1-3-1, Higashi-Hiroshima 739-8526, Japan

²Institute of Space and Astronautical Science, Japan Aerospace Exploration Agency, 3-1-1 Yoshonidai, Chuo-ku, Sagamihara, Kanagawa 252-5210, Japan

³Department of Space and Astronautical Science, School of Physical Science, The Graduate University for Advanced Studies, SOKENDAI, 3-1-1 Yoshinodai, Chuo-ku, Sagamihara, Kanagawa 252-5210, Japan

⁴Hiroshima Astrophysical Science Center, Hiroshima University, 1-3-1 Kagamiyama, Higashi-Hiroshima 739-8526, Japan

⁵The Institute of Statistical Mathematics, 10-3 Midori-cho, Tachikawa, Tokyo 190-8562, Japan

⁶DATUM STUDIO CO., LTD., Toranomon Hills 27F, 1-17-1 Toranomon, Minato-ku, Tokyo 105-6427, Japan

*E-mail: omama@astro.hiroshima-u.ac.jp, omama@ac.jaxa.jp

Received (reception date); Accepted (acceptation date)

Abstract

Simultaneous X-ray and optical observations of black hole X-ray binaries have shown that the light curves contain multiple correlated and anti-correlated variation components when the objects are in the hard state. In the case of the black hole X-ray binary, GX 339 – 4, the cross correlation function (CCF) of the light curves suggests a positive correlation with an optical lag of 0.15 s and anti-correlations with an optical lag of 1 s and X-ray lag of 4 s. This indicates the two light curves have some common signal components with different delays. In this study, we extracted and reconstructed those signal components from the data for GX 339 – 4. The results confirmed that correlation and anti-correlation with the optical lag are two common components. However, we found that the reconstructed light curve for the anti-correlated component indicates a positively correlated variation with an X-ray lag of $\sim +1$ s. In addition, the CCF for this signal component shows anti-correlations not only with the optical lag, but also with the X-ray lag, which is consistent with the CCF for the data. Therefore, our results suggest that the combination of the two positively correlated components, that is, the X-ray preceding signal with the 0.15-s optical lag and the optical preceding signal with the 1-s X-ray lag, can make the observed CCF without anti-correlated signals. The optical preceding signal may be caused by synchrotron emission in a magnetically dominated accretion flow or in a jet, while further study is required to understand the mechanism of the X-ray time lag.

Key words: X-rays: binaries — accretion, accretion disks — stars: individual (GX 339-4) — methods: statistical

1 Introduction

Black hole X-ray binaries (BHXRb) are close binary systems composed of a black-hole (BH) and a companion star. They have two major states, depending on whether X-ray emissions are soft with a high luminosity or hard with a low luminosity (Remillard & McClintock 2006). A thermal component dominates the X-ray spectrum in the soft state. In this state, it is believed that the system has an optically thick, geometrically thin disk, the so-called standard disk, which reaches to the innermost stable circular orbit (Shakura & Sunyaev 1973). In contrast, in the hard state, the X-ray spectrum is dominated by non-thermal emission. It is believed that advection-dominated accretion flow (ADAF) or jets are responsible for the non-thermal emissions (Narayan & Yi 1994, Abramowicz et al. 1994, Fender et al. 2004).

Multi-wavelength observations have revealed various time-lagged correlations between the light curves for the different wave bands in BHXRb. In the hard state, correlated X-ray and optical/near-infrared variations are occasionally observed over short time scales (0.01-10 s) (Motch et al. 1983, Kanbach et al. 2001, Hynes et al. 2009, Gandhi et al. 2008, Gandhi et al. 2010, Casella et al. 2010, Gandhi et al. 2017, Paice et al. 2019). The fast variability has common features in the cross-correlation function (CCF): a positive correlation with an optical time lag on the orders of 0.1-1.0 s and possible negative correlations with optical and/or X-ray time lags longer than the positive correlation lag (Motch et al. 1983, Kanbach et al. 2001, Durant et al. 2008, Gandhi et al. 2008, Hynes et al. 2009, Veledina et al. 2015, Paice et al. 2019). Such correlations are a key to understanding the accretion flow and jets in BHXRb.

It is possible that the reprocessing of X-rays in the outer disk makes positively correlated X-ray and optical variations with an optical lag. However, the observed time lag on the orders of 0.1-1.0 s is too short for the reprocessing scenario (e.g., Kanbach et al. 2001, Gandhi et al. 2008, Gandhi et al. 2017). Moreover, the optical delay may be explained by the travel time of electrons in the jet: the electrons generate X-rays while they are very close to the BH, but they produce optical emissions after they move downstream in the jet (Gandhi et al. 2017). The origin of the weak anti-correlations is unclear (e.g., Veledina et al. 2011, Malzac et al. 2004). It is difficult to explain them with a standard process of energy transfer, such as the reprocessing of X-rays.

The CCF gives the time lag between the correlated light curves. However, examining only the CCF makes it difficult to investigate the properties of these light curves. If the CCF indicates correlation or anti-correlation, there

should exist corresponding common signal components between X-ray and optical light curves. Extracting those signal components will provide further information on the cause of the correlated variation. In this study, we extracted the light curves for each common signal component with different time lags based on a time-frequency analysis. In our method, we assumed sparsity in the Fourier basis. This enables us to effectively select the Fourier components that are essential for the common signal components.

GX 339-4 is a BHXRb whose mass function is estimated to be $5.8M_{\odot}$ (Hynes et al. 2003, Heida et al. 2017). The object exhibits the typical CCF of X-ray and optical light curves (Gandhi et al. 2008; hereafter G08, Gandhi et al. 2010). The CCF has three extrema between -10 s and +10 s: a peak at +0.15 s, and the troughs at +1 s and -4 s, where the positive time lag is the optical lag with respect to the X-ray variation. In this work, we applied our method to the Night 1 data in G08.

In this paper, section 2 describes the data and preprocessing. The details of the signal processing are introduced in section 3. Section 4 provides the results. We discuss the implications of the results in section 5. Finally, we summarize our findings in section 6.

2 Data and preprocessing

We used the same X-ray and optical data as those for Night 1 in G08. The observation was on 18 June 2007, when the object had returned to a low-flux state after an outburst, and was in the hard state. The luminosity of 1-100 keV was $5.3 \times 10^{36} \text{ ergs}^{-1}$, corresponding to a ratio of 0.007 to the Eddington luminosity (Gandhi et al. 2010). The optical and X-ray data were obtained with the ULTRACAM attached to the Very Large Telescope and the Proportional Counter Array on the Rossi X-ray Timing Explorer satellite, respectively. The overlap duration of the observations was about an hour. The duration of the Night 1 data was 1200 s. The time interval of the data was 50 ms; thus, the number of points in each light curve is 24000. The observed optical and X-ray light curves are shown in the left panels of figure 1. In this study, we used the time t , which is the elapsed time from MJD 54269.31472020 in seconds. In the X-ray light curve, there are only $\lesssim 10$ counts, corresponding to a count rate of $\lesssim 200$, in most of the time bins after the background subtraction. Such a small number of counts means that the data contains noise due to the Poisson statistics.

The spectrograms of the observed optical and X-ray data are shown in panels (a) and (c) of figure 2. We can see significant power in the high frequency band from 2 Hz to 10 Hz in the X-ray spectrogram, although it is weak

in the optical one. The Poisson noise is dominant in the high-frequency band, compared with the common signal components. We applied a low pass filter to cut out high frequency components and noise. The filtered light curve has less Poisson noise, and we estimated the Fourier coefficients with the constrained least square method, assuming Gaussian noise. We used a finite impulse response (FIR) filter with a length of 19, a cutoff frequency of 2 Hz, and a gain less than -60 dB between 3 and 10 Hz. To cancel the phase shift caused by the FIR filter, we applied it in the forward and backward directions. Because the filter was applied twice, the gain between 3 and 10 Hz is less than -120 dB and the phase information is preserved. The same processing was applied to the optical light curve. The filtered light curves are shown in the right panels of figure 1. In panels (b) and (d) of figure 2, we show the optical and X-ray spectrograms, respectively, of the filtered light curves. We can confirm that high frequency noise is largely reduced in both datasets. We used the filtered light curves and the frequencies from 0 to 2 Hz in the following analysis.

3 Methods

3.1 Common-signal analysis

We explain how we extracted the common signal components with time lags from two observed light curves. This common signal (CS) analysis is based on the Fourier transform and thus the time lag can be estimated for each frequency. We assume the two light curves are sparse in time-frequency domain. Here, "sparse" means many coefficients of the time-frequency components are zero. Kato & Uemura (2012) reported the application of a related approach for the estimation of the power spectrum from a single light curve.

The inverse Fourier transform gives a light curve, $h(t)$, from a complex frequency sequence, $H(f)$:

$$h(t) = \int_{-\infty}^{\infty} H(f) \exp(-2\pi i f t) df. \quad (1)$$

Here, the mean in $h(t)$ is taken to be zero. Because we consider real and discrete light curves, it is rewritten as

$$h(t_i) = 2\Delta f \sum_{j=1}^M [H_R(f_j) \cos(2\pi f_j t_i) + H_I(f_j) \sin(2\pi f_j t_i)], \quad (2)$$

where each f_j is equally spaced; $\Delta f = f_{j+1} - f_j$, and $H_R(f_j)$ and $H_I(f_j)$ are the real and imaginary parts of $H(f_j)$, respectively. Here we assumed $h(t)$ does not include Fourier components other than f_1, \dots, f_M . This is simply expressed as $\mathbf{y} = \mathbf{A}\mathbf{x}$ where $\mathbf{y} = [h(t_1), \dots, h(t_N)]^T$, $\mathbf{x} = [H_R(f_1), \dots, H_R(f_M), H_I(f_1), \dots, H_I(f_M)]^T$, and

$$\begin{aligned} (A)_{i,j} &= 2\Delta f \cos(2\pi f_j t_i) \\ (A)_{i,M+j} &= 2\Delta f \sin(2\pi f_j t_i). \end{aligned} \quad (3)$$

We assume that the observed X-ray and optical light curves have common signal components. The X-ray and optical light curves, \mathbf{y}_x and \mathbf{y}_o , respectively, can be expressed with the inverse Fourier transform as described above, that is,

$$\begin{aligned} \mathbf{y}_x &= \mathbf{A}_x \mathbf{x}_x \\ \mathbf{y}_o &= \mathbf{A}_o \mathbf{x}_o, \end{aligned} \quad (4)$$

where $\mathbf{x}_x = (a_1, \dots, a_M, b_1, \dots, b_M)^T$ and $\mathbf{x}_o = (c_1, \dots, c_M, d_1, \dots, d_M)^T$ are the Fourier components, and \mathbf{A}_x and \mathbf{A}_o are the matrices of the inverse Fourier transform. Here, $\{H_R(f_j), H_I(f_j)\}$ are denoted by $\{a_j, b_j\}$ and $\{c_j, d_j\}$ for the X-ray and optical light curves, respectively. We also note that \mathbf{y}_x and \mathbf{y}_o are standardized to a zero mean and unit variance. The matrices in equation (4) can be expressed by a single equation: $\mathbf{y}_{xo} = \mathbf{A}_{xo} \mathbf{x}_{xo}$, where $\mathbf{y}_{xo} = (\mathbf{y}_x^T, \mathbf{y}_o^T)^T$, $\mathbf{x}_{xo} = (\mathbf{x}_x^T, \mathbf{x}_o^T)^T$, and

$$\mathbf{A}_{xo} = \begin{pmatrix} \mathbf{A}_x & \mathbf{O} \\ \mathbf{O} & \mathbf{A}_o \end{pmatrix}. \quad (5)$$

In CS analysis, we estimate the Fourier coefficients, \mathbf{x}_{xo} as follows:

$$\hat{\mathbf{x}}_{xo} = \arg \min_{\mathbf{x}_{xo}} \left[\|\mathbf{y}_{xo} - \mathbf{A}_{xo} \mathbf{x}_{xo}\|_2^2 + \lambda \sum_j \sqrt{a_j^2 + b_j^2 + c_j^2 + d_j^2} \right], \quad (6)$$

$$\hat{\mathbf{x}}_{xo} = \text{CS}(\mathbf{y}_{xo}), \quad (7)$$

where λ is the penalty coefficient that controls the sparsity of $\hat{\mathbf{x}}_{xo}$. The form of equation (6) is known as the group lasso (Yuan & Lin 2006). By grouping the X-ray and optical coefficients, it is expected that the coefficients become zero for the Fourier components that have high power only in either the X-ray or optical light curve, and that the relevant components of the common signals will be extracted. Note that even if the X-ray and optical signal components with the same frequency are extracted, their phases can be different because the grouped signals include sine and cosine simultaneously. Therefore, we can analyze their time lags.

In this study, we chose λ using the k -fold cross-validation method. The model was evaluated with the mean squared error yielded by the prediction from the training model on the validation dataset. We determined λ at which the mean squared error was minimized. We set $k = 10$.

Using a_j and b_j for the X-ray data, and c_j and d_j for the optical data, we can calculate the amplitudes, $Q_{x,j}$ and $Q_{o,j}$, and the phases $\phi_{x,j}$ and $\phi_{o,j}$, of a frequency, f_j as follows:

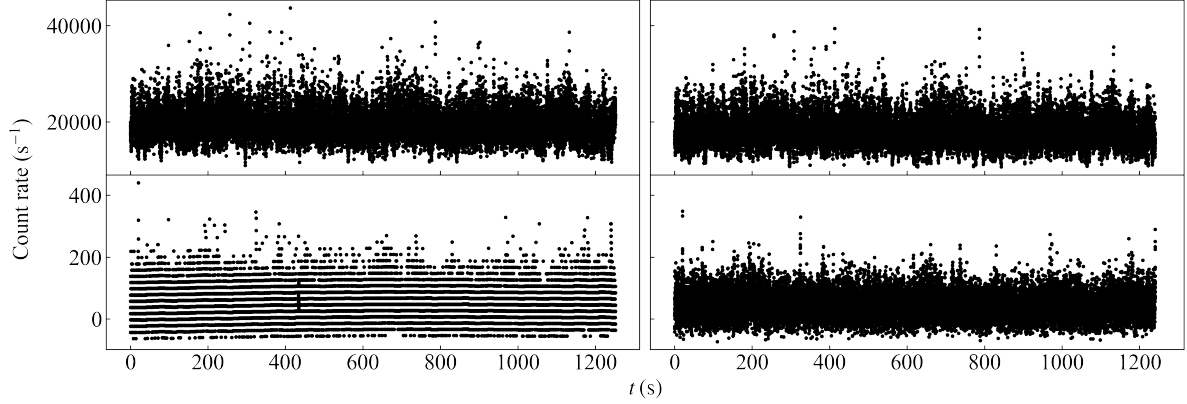


Fig. 1. Left: Observed optical (upper) and X-ray (lower) light curves. Right: Filtered optical (upper) and X-ray (lower) light curves.

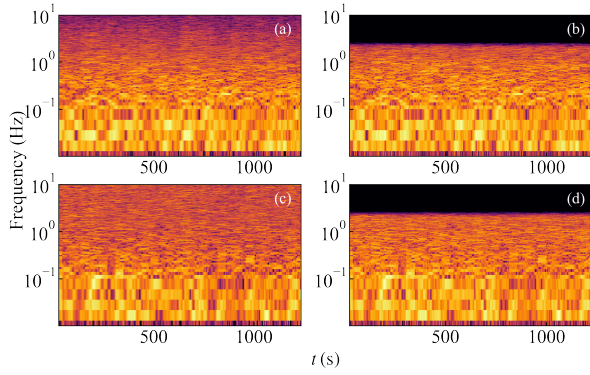


Fig. 2. Spectrograms of the original light curves and the filtered light curves. The power spectra were calculated for each short frame of 50 s. We used a Hanning window to reduce spectral leakage. Panels (a) and (c) are spectrograms of optical and X-ray original light curves, respectively. Panels (b) and (d) are spectrograms of optical and X-ray filtered light curves, respectively.

$$\begin{aligned} Q_{x,j} &= \sqrt{a_j^2 + b_j^2}, \\ Q_{o,j} &= \sqrt{c_j^2 + d_j^2}, \end{aligned} \quad (8)$$

$$\begin{aligned} \phi_{x,j} &= 2\pi f_j \Delta t_{x,j} = \arctan(b_j/a_j), \\ \phi_{o,j} &= 2\pi f_j \Delta t_{o,j} = \arctan(d_j/c_j). \end{aligned} \quad (9)$$

We obtain the time lag of the optical variation with respect to the X-ray one, τ_j , as follows:

$$\tau_j = \begin{cases} \Delta t_{x,j} - \Delta t_{o,j} & (-T_j/2 \leq \Delta t_{x,j} - \Delta t_{o,j} < T_j/2), \\ T_j/2 - (\Delta t_{x,j} - \Delta t_{o,j}) & (\text{otherwise}), \end{cases} \quad (10)$$

where T_j is the period of the j -th Fourier component, $T_j = 1/f_j$. Note that τ_j is defined as being between $-T_j/2$ and $T_j/2$.

3.2 Identification of the Fourier components for time lags

The results of CS analysis are visualized by a color-bubble plot and its histogram. An example of the plots obtained with the simulated data with $\tau = 5$ s is shown in the left

panel of figure 3. The simulated X-ray data were a sample drawn from the algorithm proposed in Timmer & Koenig (1995) where the power spectrum is expressed with a power law, and we set $P(\nu) \propto \nu^{-2}$. The optical light curve is identical to that for the X-ray curve, but with a time lag of 5 s. The sampling interval was 1 s. Each light curve has 100 data points. Both light curves were standardized to a zero mean and unit variance. In the color-bubble plot, a bubble represents the features of the Fourier component. The horizontal axis is τ , the vertical axis is $Q = \sqrt{Q_x^2 + Q_o^2}$, the color indicates the frequency, and the size indicates the amplitude ratio, that is,

$$r = \begin{cases} Q_x/Q_o & (Q_x \leq Q_o) \\ Q_o/Q_x & (Q_x > Q_o). \end{cases} \quad (11)$$

A small r means that the component has a high power only in one of the light curves and implies that it is not a common signal component. We only show components which are $r > 0.8$, thus the difference of the size is small in figure 3. In the left panel of figure 3, we can see a concentration of components at $\tau \sim 5$ s as expected.

In general, the true time lag of the j -th Fourier component is indistinguishable from its periodic counterparts, τ_j^k :

$$\tau_j^k = \tau_j + kT_j \quad (k = \dots, -1, 0, +1, \dots). \quad (12)$$

In equation (10), we define the range of τ_j as $-T_j/2 \leq \tau_j < T_j/2$. However, it is possible that the true time lag is outside this range. In the left panel of figure 3, we can see some concentrations of the Fourier components that appear due to the ambiguity in the time lag and our definition of the τ range. In addition to the concentration around the true time lag of $\tau = 5$ s, we can also see another concentration at $\tau \sim 0$ s, which apparently implies a common signal component without a significant time lag. The amplitudes of the components at $\tau \sim 0$ s are smaller

than those around the true time lag. The concentration at $\tau \sim 0$ s is made by the components of high frequencies. The right panel of figure 3 shows the bubble plot including the periodic counterparts with each T_j . We can see that most of the high-frequency components have counterparts around $\tau = 5$ s. Thus, we should select the time lag of each Fourier component from one of the periodic counterparts, and should extract Fourier components to reconstruct the light curve. When we focus on a concentration close to $\tau \sim 0$ s, it blends with the spurious concentration made by the high frequency components. In this case, we can check the significance of the concentration by a statistical test, as described in Appendix 1. In the left panel of figure 3, there is another weak concentration at $\tau \sim -3$ s, which is nearly opposite in terms of sign to the true time lag. As well as the high-frequency components around $\tau = 0$ s, most of the components around $\tau = -3$ s also have counterparts around $\tau = 5$ s, as shown in the right panel. These are the components having $T_j/2 \sim 5$ s, in which the time lag of $\tau = +5$ s is almost identical to that of $\tau = -5$ s. Hence, we should note that a hint of time lag would appear around the sign opposite to the true time lag.

We calculated τ_j assuming a positive correlation between the X-ray and optical light curves, whereas anti-correlated variations were also reported in the G08 data. The time lag in anti-correlation, τ_j^{anti} , can be obtained from τ_j and the period, T_j . When we consider a single frequency wave, for example, a positive correlation with a positive τ_j , can also be interpreted as an anti-correlation with a negative τ_j^{anti} . Thus, we obtain τ_j^{anti} by shifting τ_j by half of T_j ,

$$\tau_j^{\text{anti}} = \begin{cases} \tau_j - \frac{T_j}{2} & (\tau_j \geq 0) \\ \tau_j + \frac{T_j}{2} & (\tau_j < 0). \end{cases} \quad (13)$$

3.3 Short-time common signal analysis (STCS)

We performed the short time common-signal (STCS) analysis, in which we divided the light curves into short segments and conducted CS analysis on them. STCS analysis is essential for reconstructing the light curves when the common signals are stationary for short-time intervals but non-stationary for longer durations. This is similar to the time-frequency analysis for acoustic signal processing.

The m -th short segment, $y_m(t)$, is given from the whole light curve $y(t)$, as follows:

$$y_m(t - mS) = w_s(t - mS)y(t), \quad (14)$$

where S is the frame shift in seconds and $w_s(t)$ is the window function. Each segmented light curve has a time range of $mS \leq t < (mS + \ell)$, where ℓ is the frame length in sec-

onds. In the case of the observed data, the m -th segment can be expressed as $\mathbf{y}_m = (y_m(t_1 - mS), \dots, y_m(t_N - mS))$, where N is the number of samples in each frame. We estimate the Fourier coefficients for the m -th frame, $\hat{\mathbf{x}}_m$, with CS analysis, that is,

$$\hat{\mathbf{x}}_m = \text{CS}(\mathbf{y}_m). \quad (15)$$

We used $\ell = 50$ s, $S = 1$ s, and $N = 1000(\ell \times 20\text{Hz})$ for the data of GX 339–4 in this study. The number of frames was 1200 ($m = 1, 2, \dots, 1200$). We used the Hanning window function as $w_s(t)$. In short time Fourier analysis, window functions are employed in order to prevent power leakage in the frequency domain. The Hanning window is one of the popular window functions. We set the window size same as the length of the frame, that is, 50 s.

3.4 Reconstruction of light curves from STCS analysis

We reconstructed the common light curves with a given time lag based on the inverse Fourier transform. Each reconstructed segment is expressed as

$$\tilde{y}_m(t) = \frac{1}{N} \sum_{k \in K} \hat{x}_{m,k} \exp(2\pi i f_k t) \quad (16)$$

$$= \frac{1}{N} \sum_{k \in K} [a_k \cos(2\pi f_k t) + b_k \sin(2\pi f_k t)], \quad (17)$$

where K represents a subset of the Fourier components selected for the given time lag. The light curve is reconstructed by superposing all reconstructed segments multiplied by the weighting function, $w_a(t)$.

$$\hat{y}(t) = \sum_m w_a[t - (mS + \ell/2)] \tilde{y}_m(t), \quad (18)$$

where $t - (mS + \ell/2)$ is the middle time of each segment. We used a triangle-shaped window as $w_a(t)$:

$$w_a(t') = \begin{cases} \frac{4S}{d^2}t' + \frac{2S}{d} & (-d/2 \leq t' \leq 0) \\ -\frac{4S}{d^2}t' + \frac{2S}{d} & (0 < t' \leq d/2) \\ 0 & (\text{otherwise}), \end{cases} \quad (19)$$

where d is the length of the extracted range. Because it is known that the signals are not reliably reconstructed around the edges of each windowed frame, only the center part of $\tilde{y}_m(t)$ was used for $\hat{y}(t)$. We set $d = 2$ s.

4 Results

We performed an STCS analysis for the filtered data for GX 339–4. We show an example of the bubble plots obtained with each frame in figure 4. These are the results for the frame between $t = 615$ s and 665 s. We note that the horizontal axes of the left and right panels are τ^{anti}

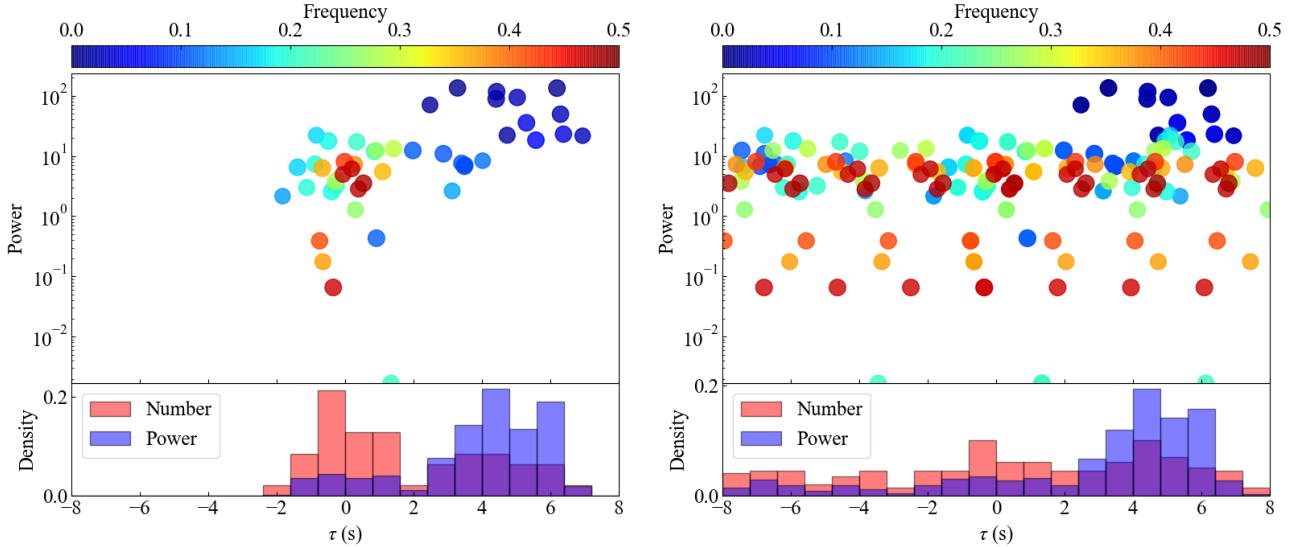


Fig. 3. Examples of the results of CS analysis. The data are the simulated set with a true time lag of 5 s. Upper panel: color-bubble plot of the Fourier components. The horizontal axis is the lag, and the vertical axis is the amplitude. The color and size of the bubbles represent the frequency and the amplitude ratio, r (for details, see the text). Lower: histogram of the Fourier components (red), and the sum of the amplitudes for each bin (blue). The left and right panels show the results without and with periodic counterparts of the components, respectively.

and τ , respectively. The figure only contains high-value r components, that is, $r > 0.8$. The dependence of the results on the threshold of r is discussed in Appendix 2. G08 reported an anti-correlation with $\tau^{\text{anti}} = +1$ s and -4 s. In the left panel, the high-frequency components are prominently concentrated at $\tau^{\text{anti}} \sim 0$ s, as described in section 3.1. In addition, weak excesses can be seen in τ^{anti} between -2.0 and -0.5 s and between $+0.5$ and $+3.0$ s. As described in section 3.1, they may correspond to a single time lag. Regarding a sub-second scale, G08 reported $\tau = 0.15$ s. In the right panel, we can see the peaks in the histogram at $\tau \sim 0.25$ s and -0.2 s. They may correspond to a single time lag of $\tau = 0.15$ s in G08.

Figure 5 shows the temporal variation of the time lag obtained from the STCS analysis. The horizontal and vertical axes are t and τ or τ^{anti} , respectively. The color indicates the total amplitude of the Fourier components in each bin, which is equivalent to the blue boxes in the bubble plot. We call such a plot a time lag map in this paper. Panels (a) and (c) show the time lag map in τ and τ^{anti} , respectively. We masked the time lag between -0.8 and 0.8 s to emphasize the second-scale time lags. No clear concentration of the components can be seen in the maps, whereas some intermittent concentrations are evident at $\tau^{\text{anti}} \sim 0.5$ – 2.5 s in panel (c). This concentration range corresponds to the anti-correlation with the optical lag of $+1$ s reported in G08. We note that there are no hints of component concentrations at $\tau^{\text{anti}} \sim -4$ s, which was reported in G08. Panels (b) and (d) are the same as panels (a) and (c), but for sub-second time lags. We can see

more components in the region between $\tau = 0.1$ s and 0.3 s than those between $\tau = -0.1$ and -0.3 s in panel (b). This asymmetry of the distribution corresponds to the time lag of $\tau = 0.15$ s reported in G08. In contrast, in panel (d), there is an opposite asymmetry of the distribution. They may be the same common signal component if the time scale of the signal is almost double that of the time lag.

We extracted the Fourier components for the two common signal components, and reconstructed their light curves. In order to test the reliability of the reconstructions, we evaluated the distribution of each point of the light curve via resampling. We randomly selected K samples from N observed data points and repeated it for M times. The resulting fluctuation of the reconstructed point gives the estimation of the distribution. The result is shown in figure 6 where $M = 100$ and $K/N = 0.5$. First, we reconstructed the light curve from the Fourier components around $\tau = +0.1$ s, which were extracted by using the significance test described in Appendix 1. We used τ in a range between -0.8 and $+0.8$ s for the test. Parts of a reconstructed light curve are shown in figure 6 as orange curves. We can see that the optical variation is delayed by $\sim +0.1$ s compared with the X-ray variation, as expected.

Second, we extracted all the components between $\tau^{\text{anti}} = +0.5$ and $+2.5$ s for the reconstruction of the light curves of $\tau^{\text{anti}} \sim +1$ s. We also extracted the periodic counterparts of the other components that lie in this τ^{anti} region. Parts of the reconstructed light curve are shown by the blue curves in figure 6. We found that, although we extracted the components with a positive τ^{anti} , the re-

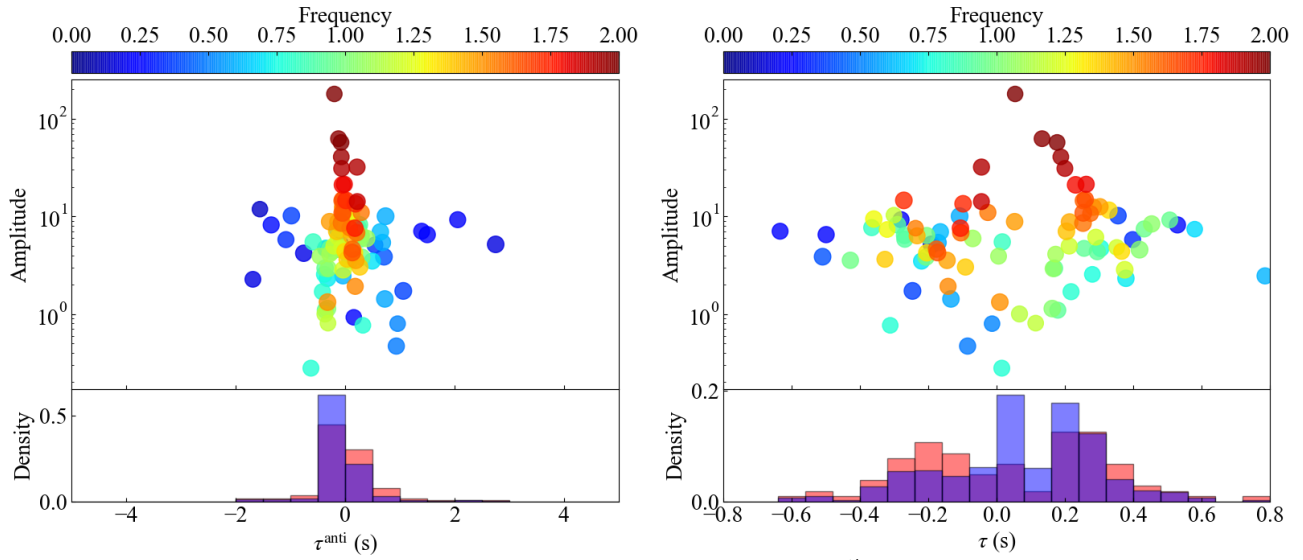


Fig. 4. Bubble plots for the frame $t = 615$ -665. The horizontal axes of the left and right panels are τ^{anti} and τ , respectively.

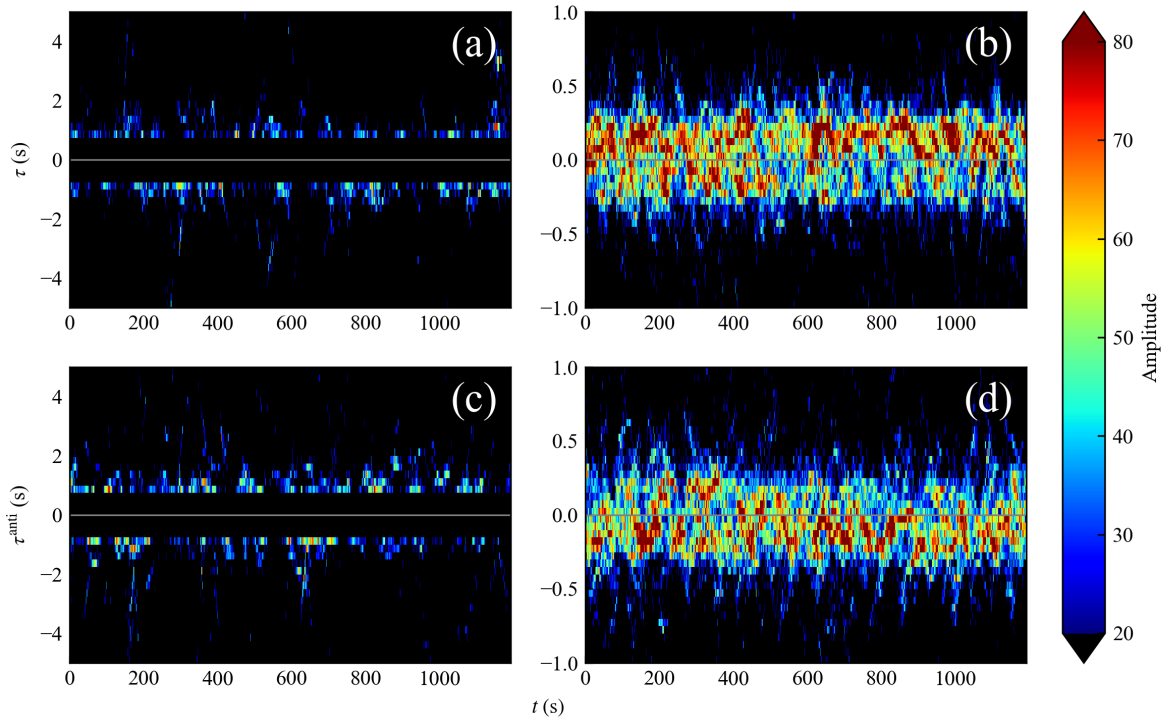


Fig. 5. Time lag maps obtained with the STCS analysis. The vertical axes indicate τ and τ^{anti} in panels (a), (b), and (c), (d), respectively. The color represents the total amplitude in each bin. We masked the band between -0.8 and 0.8 s in panel (a) and (c) to emphasize the structure in the region of long time lags.

constructed light curve can be interpreted as a positively correlated variation with an X-ray delay, that is, $\tau \sim -1$ s.

Thus, our analysis suggests that the observed light curves include two common signal components having $\tau \sim +0.1$ s and $\tau \sim -1$ s. The signal component of $\tau = +0.1$ s means that the X-ray variation precedes the optical variation, thus, we call it the X-ray preceding signal (XPS). Likewise, the component of $\tau = -1$ s is called optical preceding signal (OPS).

The power spectrum densities (PSDs) for the XPS and OPS in the optical band are shown in figure 7 with orange and blue curves, respectively. The peak frequencies are ~ 2 Hz and ~ 0.2 Hz in PSDs of the XPS and OPS, respectively. We note that the frequency of the XPS only gives a lower limit of the characteristic frequency because the FIR filter has a cutoff frequency of 2 Hz. Hence, the characteristic time scale of the XPS and OPS are estimated to be < 0.5 s and ~ 5 s, respectively.

We show the whole X-ray light curves for the XPS and OPS in figure 8. The figure includes the time variation of the standard deviation (SD) of the light curve in each 50-s frame. We can see that the active periods for the XPS are different from those for the OPS. The OPS active periods appear to precede the XPS activity. In contrast, the time scale of the SD variation seems to be identical in both the XPS and OPS, at about 100 s. We checked that the optical light curves have similar features to the X-ray curves.

5 Discussion

5.1 Cross-correlation function of XPS and OPS

The CCF for the filtered light curves is shown in panel (a) of figure 9, and the CCFs for the XPS and OPS are shown in panel (b). The time lag is defined as the optical delay with respect to the X-ray variation. The CCF for the XPS has a single peak at a lag of 0.1 s. The CCF for the OPS has a single peak at a lag of -1 s and trough at a lag of 1 s. These CCF patterns for the XPS and OPS are expected from the reconstructed light curves shown in figure 6. In order to see the reliability of the correlation coefficient, we randomly picked up 100 reconstructed light curves obtained with the resampling method and evaluated the fluctuation empirically. As a result, we see that the 90% confidence intervals of the coefficients were less than 0.1. In addition, the CCF for the OPS also has a small trough at -3 s, which is consistent with the anti-correlated signal reported in G08. Adding the reconstructed light curves for the XPS to those for the OPS, we made combined light curves for the X-ray and optical emissions. The CCF for the combined light curves is shown in panel (c) of figure

9. The CCF reproduces the major features of the filtered curve, that is, the peak at $+0.1$ s and the trough at $+1$ s. In addition, the original CCF has relatively high correlation coefficients between -2 and 0 s, which is reproduced in panel (c) due to the contribution of the OPS. Thus, we conclude that the two positively correlated signal components, that is, the XPS and OPS, made the original CCF, including the apparently anti-correlated patterns.

Gandhi et al. (2010) performed a cross-spectrum analysis for the data. Their time lag spectrum shows optical preceding components between ~ 0.8 and 0.3 Hz without high coherence. The components presumably correspond to the OPS that we found. Hence, the result of their cross-spectrum analysis supports the presence of the OPS.

A possible discrepancy between the CCFs is the correlation coefficient for the lag of > 3 s; it is significantly positive in panel (a), whereas it is almost zero in panel (c). This implies that the observed light curves include variations with a longer time scale and time lag than those discussed here. The systematically high correlation coefficients may cause the relatively shallow trough at $+1$ s in panel (a) compared with that in panel (c). The anti-correlation with a lag of -3 s may be reproduced by the OPS, as shown in panel (b), whereas the noise in the CCF for the XPS disturbs this feature in the combined CCF. After constructing the light curves from the common components, we subtracted them from the original filtered light curves and made the residual light curves of the X-ray and optical emissions. The CCF for the residual light curves is shown in panel (d). The trough at $+1$ s disappears in panel (d) because the OPS is subtracted. We can see that the negative correlation at -3 s does not completely disappear in panel (d), nor does the XPS peak at $+0.15$ s. These residual correlations imply that the amplitudes of the XPS and OPS are underestimated in our analysis. A part of the common signals may remain in the residual light curves even after our analysis.

5.2 Physical interpretation of OPS

So far, it has been believed that the observed X-ray and optical light curves include anti-correlated variations, as indicated by the CCF. The complex shape of the CCF can be interpreted with two components, a broad anti-correlation component at a lag of ~ 0 s and a sharp positive correlation peak at a lag of a few subseconds (Gandhi et al. 2008, Durant et al. 2011). There are two major explanations for the anti-correlation (e.g., Uttley & Casella 2014, and references therein). One of them appeared in Veledina et al. (2011), where they explained that the optical emission is the synchrotron emission from a hot accretion flow

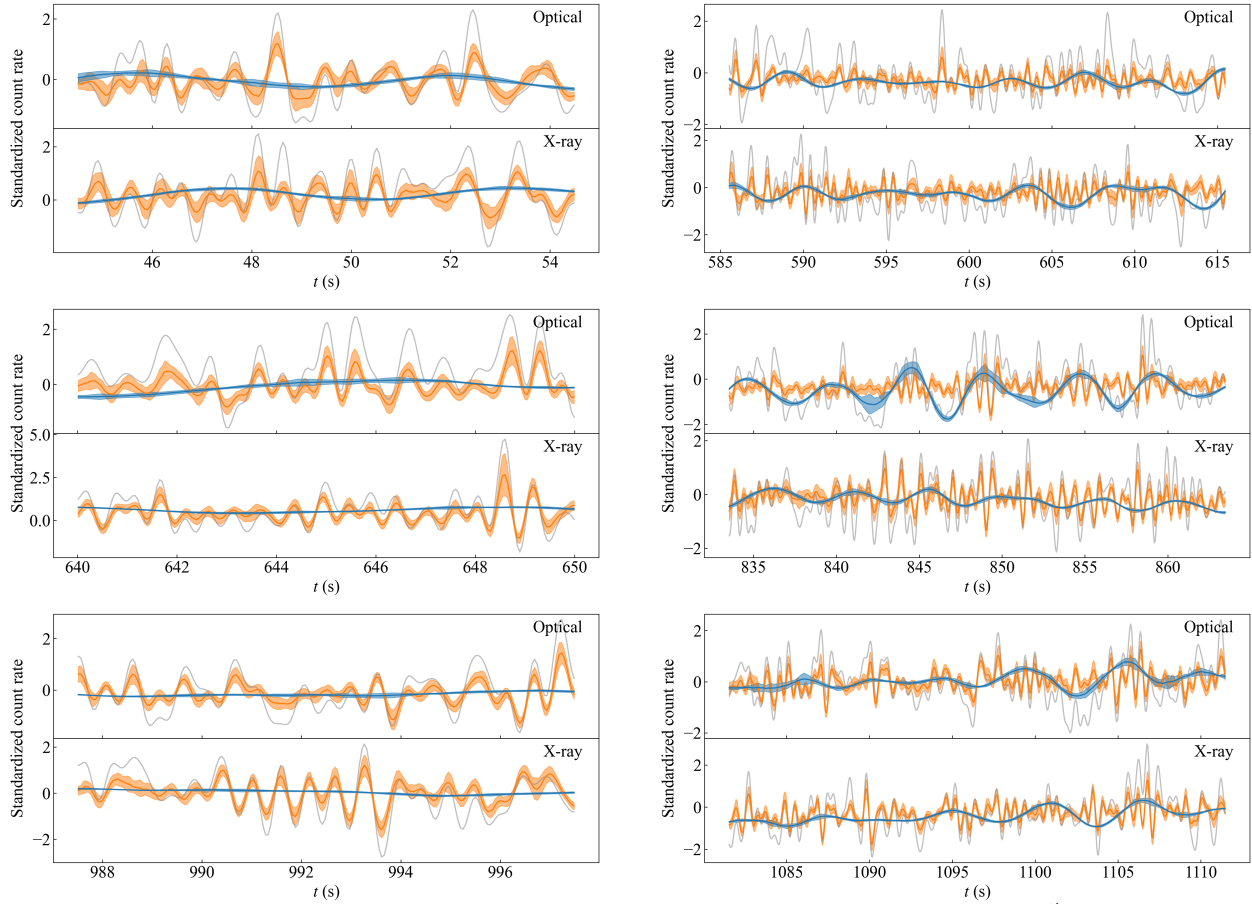


Fig. 6. Reconstructed light curves. The orange, blue, and grey curves are the reconstructed light curve of $\tau = +0.1$ s and $\tau^{\text{anti}} = +1$ s, and filtered light curves, respectively. The shaded area represents the 90 % confidence interval which is evaluated via resampling. The upper and bottom parts of each panel are the optical and the X-ray light curves, respectively. The left panel has a short range of 10 s, in which the variation of $\tau = +0.1$ is clearly seen. The right panel has a long range of 30 s, in which the variation of $\tau^{\text{anti}} = +1$ s is clearly seen. The count rate of OPS is magnified by 1.5 times to see variations clearly.

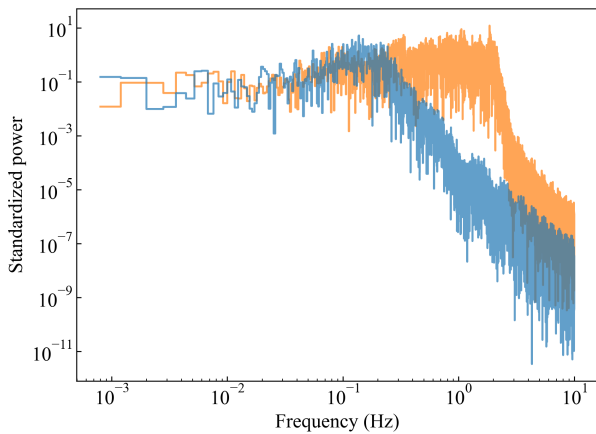


Fig. 7. Power spectrum densities of the XPS and OPS in the optical band, indicated by orange and blue curves, respectively.

and the Comptonization of the synchrotron radiation that is dominant in the X-ray regime. According to their scenario, the optical decay occurs because of the synchrotron self-absorption effect (Veledina et al. 2017). The other major explanation appeared in Malzac et al. (2004), where they explained that the X-ray and optical emission share the common energy reservoir, which leads to their anti-correlation. According to these explanations, the X-ray emission comes from the corona above the accretion disk, and the optical emission comes from the jet. The X-ray flux increases when the corona receives much energy from the reservoir. The optical flux increases after the accreting gas drops into the inner region, and transfers energy to the jet.

Our results suggest that there is no anti-correlation but a positive correlation with an optical lag of ~ 0.1 s (XPS) and a positive correlation with an X-ray lag of ~ 1 s (OPS). Gandhi et al. (2017) found that the optical variation in V404 Cyg was delayed with respect to the X-ray variation by ~ 0.1 s. Their explanation was that its optical

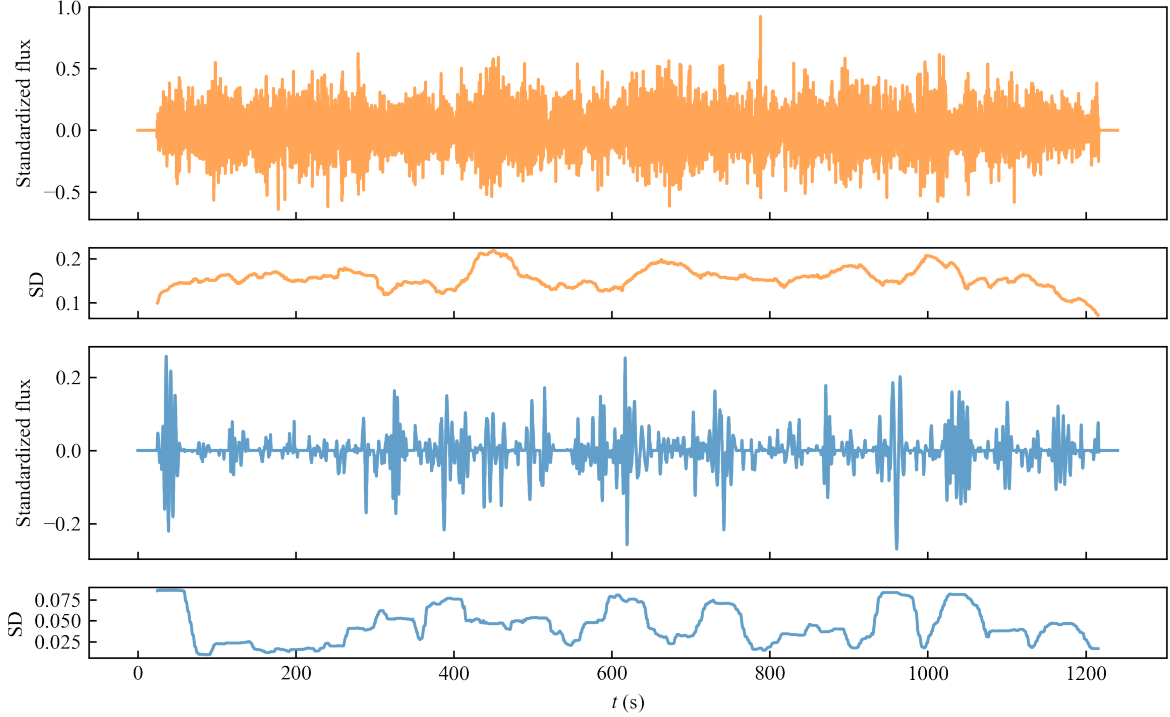


Fig. 8. Reconstructed X-ray light curves for the XPS and OPS, and the time variation in the standard deviation (SD) of each frame. The orange curves show the XPS light curve and its SD. The blue curves show the OPS light curve and its SD.

emission originates from the jet, and the optical time lag corresponds to the electron travel time from the base of the jet to the optical emission region. The XPS in GX 339 – 4 has characteristic features in common with the short-term variation in V404 Cyg, and they probably have the same nature. Here, we consider different physical models of the OPS. The asynchronous nature of the active periods of XPS and OPS, as shown in figure 8, indicates that the source of the OPS is distinct from that of the XPS.

First, we consider a typical situation for the hard state: the optical emission is the thermal radiation from the standard disk, and the X-ray emission is from ADAF. If the time scale of 5 s corresponds to the dynamical time scale of the standard disk, $t_{\text{dyn}} = 2\pi r^{2/3} \sqrt{GM}$, the distance between the optical source and the central BH is $r \sim 10^3 R_s$ (where $R_s = GM/c^2$) for a BH mass of $M = 6M_\odot$ (Hynes et al. 2003). This distance provides an upper limit on the size of ADAF. The time lag of 1 s may be explained by the inward free fall of the optical source in ADAF. The truncated radius of the disk is theoretically predicted to be between $10^2 R_s$ and $10^4 R_s$ (Esin et al. 1997), which is consistent with the above scenario. However, it is difficult to reproduce the observed amplitude of the OPS with such an inner, small emitting source because the thermal emission from the outer disk ($\sim 10^5 R_s$) dominates the optical

emission.

Second, we consider a situation in which the optical emission is synchrotron radiation from the inner accretion flow. Strong synchrotron emissions are expected in magnetically dominated accretion flow (MDAF), in which electrons can be accelerated at the site of the magnetic reconnection (Dal Pino et al. 2010, Khiali et al. 2015). In this scenario, the origin of the X-ray time lag is uncertain. Possibly, the X-ray emission is generated by the inverse-Compton scattering of synchrotron emission at the corona, which is distant from the optical source. The location of the optical source can be estimated, in the same way as above, to be $\sim 10^3 R_s$. The time lag of 1 s corresponds to $\sim 10^4 R_s$ if we consider it as the light travel time. However, both distances are much larger than those expected for the sizes of MDAF and hot corona ($\lesssim 10 R_s$).

Kalamkar et al. (2016) investigate the correlation between X-ray and infrared light curves and found X-ray lagged signal. Malzac et al. (2018) interpreted this as a result of internal shocks generated by the collisions of plasma shells. In this model, the infrared flux depends on the difference of the Lorentz factors of the colliding shells. Hence, on long time-scales, it corresponds to the time derivative of the jet Lorentz factor which can be traced by the X-ray flux. It leads to a positive correlation with $-\pi/2$ phase

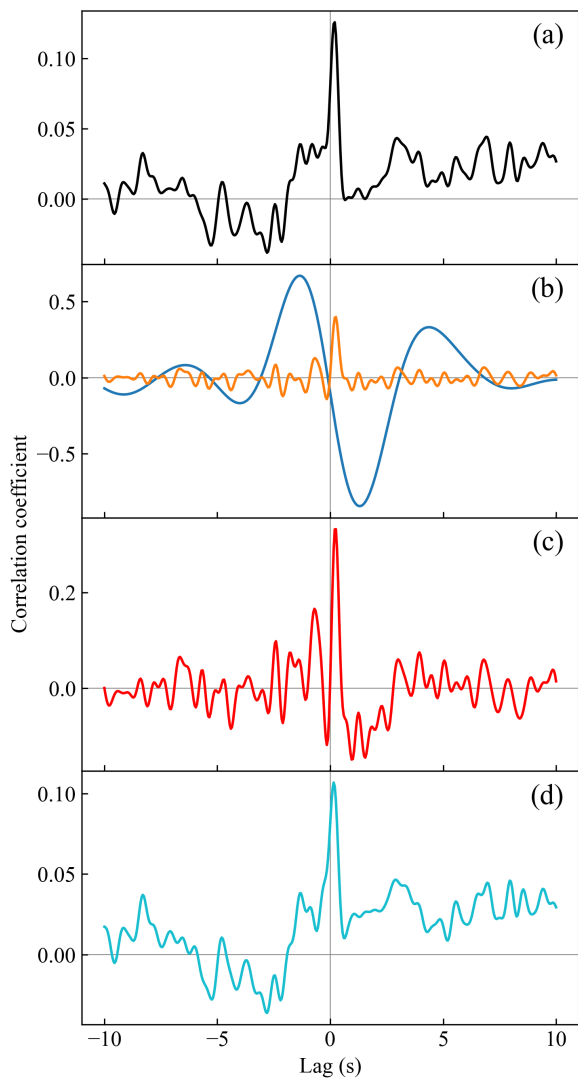


Fig. 9. (a) CCF for the filtered light curves. (b) CCFs for the reconstructed light curves for the XPS (orange) and OPS (blue). (c) CCF for the combined light curves for the XPS and OPS. (d) CCF for the residual light curves.

shift of the infrared signal to the X-ray one. According to this scenario, we can also expect a negative correlation with a $+\pi/2$ phase shift when we consider a periodic signal as we know from the CCF for OPS. The two strong positive/negative correlations seen in the CCF of OPS in panel (b) of figure 9 may support the scenario.

6 Summary

This paper describes a study of the signal propagation between two light curves of different wavelengths. More precisely, common signal components were extracted from the X-ray and optical light curves of GX 339–4. Our method is based on the short time Fourier analysis, and it assumes the sparsity in the power spectrum to effectively extract

common signal components from noisy data. We detected two common signal components: one is that correlates with a 0.15-s optical lag and the other is that anti-correlates with a 1-s optical lag. We found that the reconstructed light curve for the anti-correlated component showed a positive correlation with a 1-s X-ray time lag. Hence, our explanation is that the data contain two positive correlated signal components, that is, the XPS and OPS. Our results demonstrate that combining the XPS and OPS reproduces the CCF for the data. The short time scale and large variation amplitude of the OPS suggest that the optical source of the OPS is not the thermal disk, but rather the inner MDAF or in a jet.

Acknowledgments

The authors appreciate Prof. Poshak Gandhi, who kindly shared data with us and gave useful comments on this paper.

Appendix 1 Significance test for the concentration of the Fourier components

As mentioned in section 3.1, the CS analysis makes a spurious concentration of the high-frequency components around $\tau = 0$ s. We employed a significance test to extract the Fourier components of a common signal with $\tau \sim 0$ s. The null hypothesis of the test is that the Fourier components selected by the CS analysis provide a totally uncorrelated signal. In other words, the phase lag of each component should be uniformly random between $-\pi$ and π . We can obtain the distribution of the number of components in each time lag bin by resampling the phase lag of the components. Using the simulated data that are described in section 3.1, we show the resampling distribution of the number of components between $\tau = 1$ and 2 s in the left panel of figure 10. The observed number of components represented by the red line is almost at the peak of the distribution, which means that we cannot reject the null hypothesis. In this case, we can reject the null-hypothesis with a 95% confidence level if the number of components is larger than 14. We show a histogram of the components and the 95% confidence level for each lag bin with the dashed curve in the right panel of figure 10. We can conclude that the concentration of components at $\tau \sim 5$ s is significant at a 90% of confidence level. We note that the test is unreliable when the number of components in a time lag bin is small.

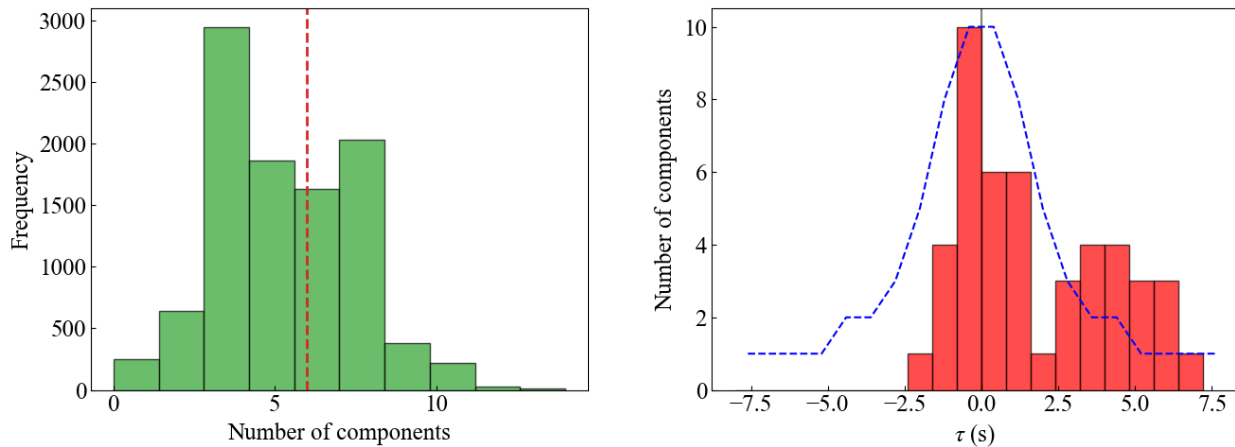


Fig. 10. Examples of the significance test. The data are the same as the simulated data used in section 3.1, which have a true lag of $\tau = 5$ s. Left: The resampling distribution of the number of components between $\tau = 1$ to 2 s. The dashed red line indicates the observed number of components. Right: The histogram of components, which is the same as the red bins in the left panel of figure 3. The blue curve indicates the 90% confidence level.

Appendix 2 Relation between r and CCF

In the CS analysis, the reconstructed light curves depend on the parameter of the amplitude ratio, r . In the main text, we used $r = 0.8$. Here, we discuss the dependency of the results on r . The CCF for the filtered light curves is shown in panel (a) of figure 11. The CCF for the residual light curves obtained with $r = 0.0$ is shown in panel (b). The residual CCFs with $r = 0.7, 0.8, 0.9$ are shown in panel (c) with blue, orange, and green curves, respectively. The orange curve is the same as the CCF in panel (d) of figure 9. While we can see a dip around a lag of 1.0 s in the CCF of panel (a), the CCF rather has a positive peak there in panel (b). In panel (c), the dip is correctly removed in all residual CCFs. These results suggest that the reconstructed light curves with small r , such as $r = 0.0$, contain a lot of non-common components which cause an over-fitting for the common signal with a lag of ~ 1.0 s. Hence, r should be large enough to remove such non-common components. The dependence of the results on r is small at $r > 0.7$.

References

- Abramowicz, M. A., Chen, X., Kato, S., Lasota, J.-P., & Regev, O. 1994, arXiv preprint astro-ph/9409018
- Casella, P., Maccarone, T., O'Brien, K., Fender, R., Russell, D., Van Der Klis, M., Pe'Er, A., Maitra, D., et al. 2010, *Monthly Notices of the Royal Astronomical Society: Letters*, 404, L21
- Dal Pino, E. d. G., Piovezan, P., & Kadowaki, L. 2010, *Astronomy & Astrophysics*, 518, A5
- Durant, M., Gandhi, P., Shahbaz, T., Fabian, A. P., Miller, J., Dhillon, V., & Marsh, T. R. 2008, *The Astrophysical Journal Letters*, 682, L45
- Durant, M., Shahbaz, T., Gandhi, P., Cornelisse, R., Munoz-Darias, T., Casares, J., Dhillon, V., Marsh, T., et al. 2011, *Monthly Notices of the Royal Astronomical Society*, 410, 2329
- Esin, A. A., McClintock, J. E., & Narayan, R. 1997, *The Astrophysical Journal*, 489, 865
- Fender, R. P., Belloni, T. M., & Gallo, E. 2004, *Monthly Notices of the Royal Astronomical Society*, 355, 1105
- Gandhi, P., Bachetti, M., Dhillon, V. S., Fender, R. P., Hardy, L. K., Harrison, F. A., Littlefair, S. P., Malzac, J., et al. 2017, *Nature Astronomy*, 1, 859
- Gandhi, P., Dhillon, V. S., Durant, M., Fabian, A. C., Kubota, A., Makishima, K., Malzac, J., Marsh, T. R., et al. 2010, *Monthly Notices of the Royal Astronomical Society*, 407, 2166–2192
- Gandhi, P., Makishima, K., Durant, M., Fabian, A., Dhillon, V., Marsh, T., Miller, J., Shahbaz, T., & Spruit, H. 2008, *Monthly Notices of the Royal Astronomical Society: Letters*, 390, L29
- Heida, M., Jonker, P., Torres, M., & Chiavassa, A. 2017, *The Astrophysical Journal*, 846, 132
- Hynes, R., Brien, K. O., Mullally, F., & Ashcraft, T. 2009, *Monthly Notices of the Royal Astronomical Society*, 399, 281
- Hynes, R. I., Steeghs, D., Casares, J., Charles, P., & O'Brien, K. 2003, *The Astrophysical Journal Letters*, 583, L95
- Kalamkar, M., Casella, P., Uttley, P., O'Brien, K., Russell, D., Maccarone, T., van der Klis, M., & Vincentelli, F. 2016, *Monthly Notices of the Royal Astronomical Society*, 460, 3284
- Kanbach, G., Straubmeier, C., Spruit, H., & Belloni, T. 2001, *Nature*, 414, 180
- Kato, T. & Uemura, M. 2012, *Publications of the Astronomical Society of Japan*, 64
- Khiali, B., de Gouveia Dal Pino, E. d., & del Valle, M. V. 2015, *Monthly Notices of the Royal Astronomical Society*, 449, 34
- Malzac, J., Kalamkar, M., Vincentelli, F., Vue, A., Drapeau, S., Belmont, R., Casella, P., Clavel, M., et al. 2018, *Monthly Notices of the Royal Astronomical Society*, 480, 2054
- Malzac, J., Merloni, A., & Fabian, A. C. 2004, *Monthly Notices*

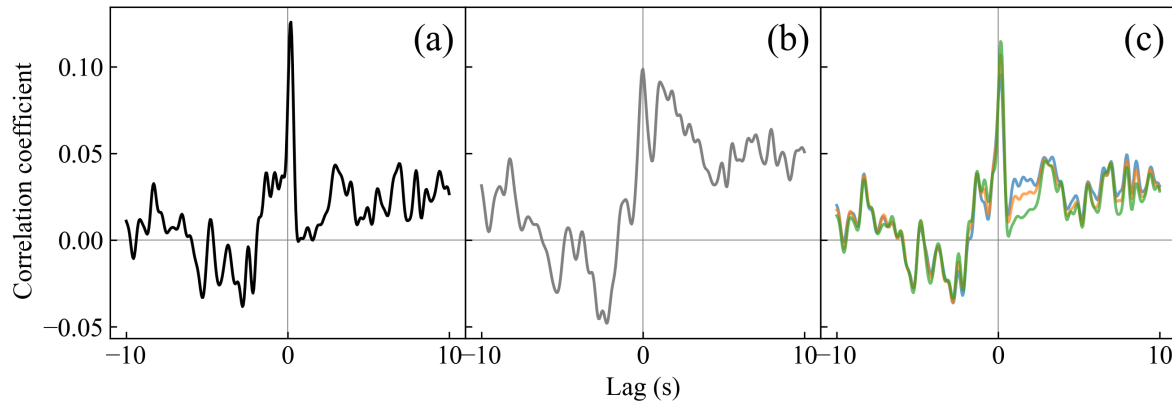


Fig. 11. (a) CCF for the filtered light curves. (b) CCFs for the reconstructed light curves which $r = 0.0$. (c) CCF for the reconstructed light curves which $r = 0.7, 0.8, 0.9$, indicated by blue, orange, and green, respectively.

of the Royal Astronomical Society, 351, 253

Motch, C., Ricketts, M., Page, C., Ilovaisky, S., & Chevalier, C.

1983, *Astronomy and Astrophysics*, 119, 171

Narayan, R. & Yi, I. 1994, arXiv preprint astro-ph/9403052

Paice, J., Gandhi, P., Shahbaz, T., Uttley, P., Arzoumanian, Z., Charles, P., Dhillon, V., Gendreau, K., et al. 2019, *Monthly Notices of the Royal Astronomical Society: Letters*, 490, L62

Remillard, R. A. & McClintock, J. E. 2006, *Annu. Rev. Astron. Astrophys.*, 44, 49

Shakura, N. I. & Sunyaev, R. A. 1973, *Astronomy and Astrophysics*, 24, 337

Timmer, J. & Koenig, M. 1995, *Astronomy and Astrophysics*, 300, 707

Uttley, P. & Casella, P. 2014, *Space Science Reviews*, 183, 453

Veledina, A., Gandhi, P., Hynes, R., Kajava, J. J., Tsygankov, S. S., Revnivtsev, M. G., Durant, M., & Poutanen, J. 2017, *Monthly Notices of the Royal Astronomical Society*, 470, 48

Veledina, A., Poutanen, J., & Vurm, I. 2011, *The Astrophysical Journal Letters*, 737, L17

Veledina, A., Revnivtsev, M. G., Durant, M., Gandhi, P., & Poutanen, J. 2015, *Monthly Notices of the Royal Astronomical Society*, 454, 2855

Yuan, M. & Lin, Y. 2006, *Journal of the Royal Statistical Society: Series B (Statistical Methodology)*, 68, 49